IOP Publishing Journal of Physics: Condensed Matter
J. Phys.: Condens. Matter **34** (2022) 265001 (13pp) https://doi.org/10.1088/1361-648X/ac64df

Nanoscale pattern formation on silicon surfaces bombarded with a krypton ion beam: experiments and simulations

J Seo[1], D A Pearson[2], R M Bradley[3] and J-S Kim[1,4,*]

[1] Institute of Advanced Materials and Systems, Sook-Myung Women's University, Seoul, 04310, Republic of Korea
[2] Division of Science and Engineering, Pennsylvania State University, Abington, Abington, PA 19001, United States of America
[3] Departments of Physics and Mathematics, Colorado State University, Fort Collins, CO 80523, United States of America
[4] Department of Physics, Sook-Myung Women's University, Seoul 04310, Republic of Korea

E-mail: jskim@sookmyung.ac.kr

Received 1 February 2022, revised 21 March 2022
Accepted for publication 6 April 2022
Published 27 April 2022

Abstract

The nanoscale patterns produced by bombardment of the (100) surface of silicon with a 2 keV Kr ion beam are investigated both experimentally and theoretically. In our experiments, we find that the patterns observed at high ion fluences depend sensitively on the angle of incidence Θ. For Θ values between 74° and 85°, we observe five decidedly different kinds of morphologies, including triangular nanostructures traversed by parallel-mode ripples, long parallel ridges decorated by short-wavelength ripples, and a remarkable mesh-like morphology. In contrast, only parallel-mode ripples are present for low ion fluences except for $\Theta = 85°$. Our simulations show that triangular nanostructures that closely resemble those in our experiments emerge if a linearly dispersive term and a conserved Kuramoto–Sivashinsky nonlinearity are appended to the usual equation of motion. We find ridges traversed by ripples, on the other hand, in simulations of the Harrison–Pearson–Bradley equation (Harrison *et al* 2017 *Phys. Rev.* E **96** 032804). For $\Theta = 85°$, the solid surface is apparently stable and simulations of an anisotropic Edwards–Wilkinson equation yield surfaces similar to those seen in our experiments. Explaining the other two kinds of patterns we find in our experiments remains a challenge for future theoretical work.

Keywords: nanoscale patterns, ion bombardment, silicon surface

(Some figures may appear in colour only in the online journal)

1. Introduction

Ion beam irradiation (IBI) with an ion energy between 10 and 10^5 eV can produce self-assembled patterns of dots or ripples on most solid surfaces. This observation has raised questions regarding the physical mechanisms that lead to the self assembly. It has also led to a great deal of interest in the possible applications of IBI that exploit its scalable, single-step, low-cost nano-patterning capabilities [1–4].

Silicon targets have taken center stage in the study of nanopatterning by IBI. That is in part because of the ease of analysis, because at room temperature an initially crystalline Si target becomes amorphous near the surface during IBI, obviating the need to consider the anisotropic kinetic and energetic processes that act on crystalline surfaces, and in part because

* Author to whom any correspondence should be addressed.

 © 2022 IOP Publishing Ltd Printed in the UK

of silicon's importance in modern industrial applications [5, 6].

A consensus seems to have been reached on the pattern evolution on Si as the angle of incidence Θ is increased [7–11]. (Θ is the polar angle of the ion beam measured with respect to the surface normal.) Below the threshold angle for pattern formation $\Theta_{\rm th}$, the surface is stable and it remains almost completely flat. (The value of $\Theta_{\rm th}$ depends on the choice of ion beam. It is approximately equal to 55° in our experiments.) For $\Theta_{\rm th} < \Theta < \Theta_{\rm r} \sim 80°$, a parallel-mode ripple pattern develops with its wave vector parallel to the surface projection of ion beam's direction. Moreover, at least according to the consensus, for $\Theta > \Theta_{\rm r}$, a perpendicular-mode ripple pattern prevails with its wave vector perpendicular to the surface-projected ion beam direction. At $\Theta_{\rm r}$, the instability is biaxial, and mounds form on the surface. This apparent reorientation of the ripple pattern is rather insensitive to the incident ion energy E if $E \leqslant 2$ keV, and is also observed for Ge [12–14] and mica [15] targets. A switch from parallel-mode to perpendicular-mode ripples as Θ is increased is predicted by the Bradley–Harper theory, the first theory that was able to explain the genesis of rippled topographies on surfaces subjected to IBI [7]. The equation of motion (EOM) that describes the surface dynamics is commonly taken to be the anisotropic Kuramoto–Sivashinsky (AKS) equation [5, 16].

Difficulties with this conventional viewpoint have started to become increasingly evident. The nature of the so-called perpendicular-mode ripple pattern is controversial because the patterns show little order as judged by the absence of the expected peaks in their power spectral densities [17]. The kinds of patterns that are observed in experiments are also more diverse than those mentioned above. Raised and depressed triangular regions that are traversed by parallel-mode ripples are frequently observed [5, 11, 12, 18–27], for example, although typically little attention has been paid to them. Terraced surfaces and 'fins' (tilted ridges that are aligned with the projected ion beam direction) form in other experiments [12, 13, 18, 22, 28–38]. The AKS equation does not produce triangular nanostructures, terraces or fins. Loew and Bradley [39] recently found that once the effect of linear dispersion has been added to the AKS equation, triangular nanostructures develop. On the other hand, the addition of cubic nonlinearities to the AKS equation results in the Harrison–Pearson–Bradley (HPB) equation, which yields terraces and fins similar to the ones seen in many experiments [40, 41].

In this paper, we study the nanoscale patterns that develop on the (100) surface of silicon when it is irradiated with a 2 keV Kr ion beam. Our work complements and extends earlier experimental studies with this ion-target combination [9, 37]. We find that the patterns observed at high ion fluences depend sensitively on the angle of incidence. In particular, for angles of incidence between 74° and 85°, we observe five distinctly different kinds of topographies—triangular nanostructures traversed by ripples, complex terraced structures, fins decorated by parallel-mode ripples, an intriguing mesh-like morphology, and a so-called perpendicular-mode ripple pattern. In contrast, only parallel-mode ripples are present for low ion fluences except for $\Theta = 85°$. In the latter case, the solid surface is apparently stable, and roughens only as a result of shot noise in the ion beam. We also place our experimental results in the context of theories developed since the earlier experimental work on the bombardment of silicon with a 2 keV Kr ion beam was carried out. Triangular nanostructures that closely resemble those in our experiments emerge if a conserved Kuramoto–Sivashinsky nonlinearity is appended to the EOM studied by Loew and Bradley. Fins traversed by parallel-mode ripples, on the other hand, are found in simulations of the HPB equation for a range of parameter values. 'Perpendicular-mode ripples' akin to those we observe experimentally are also reproduced in our simulations. Complex terraced surfaces and mesh-like morphologies did not develop in simulations of any of the equations of motion we have examined, however. As such, they represent a challenge to future theoretical work.

This paper is organized as follows. We discuss the details of our experimental set-up in section 2. Our experimental results for a range of ion fluences and incidence angles are presented in section 3. Our observations are compared with existing theoretical models in section 4 and some improvements to these models are advanced. In section 5, we compare our experimental results with past studies of IBI of silicon with a 2 keV Kr ion beam. Finally, in section 6, we summarize the results of our investigations, in part by giving a 'phase diagram' of patterns as a function of incidence angle and fluence that represents a more refined and complete version of previous diagrams.

2. Experimental details

IBI was performed in a vacuum chamber with a base pressure in the low 10^{-9} Torr range. B-doped, 10 mm × 10 mm Si(100) chips were irradiated by a 2 keV Kr ion beam employing a Kauffman-type ion gun (Physical Electronics, 04-161 Sputter Ion Gun). The (global) beam flux (f) estimated from the total beam current was $f \sim 10$ μA cm^{-2} at $\Theta = 0°$. Since secondary electrons also contribute to the beam current, f only sets an upper limit on the real ion flux. Θ was adjusted by an a.c. servo motor controlled by a LabView program we built.

The patterns formed on the Si substrate were imaged *ex situ* by an atomic force microscope (AFM; Park Systems XE-100) in the non-contact mode. The images were then analyzed using both the SPIP package (Image Metrology) and home-built programs.

The ion gun was operated in the fully focused mode so that the beam diameter was less than 10 mm. A photograph that gives an indication of the beam cross-section at the surface is shown in figure 1(a) for a case in which the beam was obliquely incident on the sample. Figure 1(b) shows a contour map of the surface width W measured by AFM. The beam center, which was defined to be the surface point with the greatest value of f and W, was used as the reference position for the purpose of specifying a value of Θ. We place the origin of the coordinate system at the beam center, the x axis in the same direction as the surface projection of the ion beam direction, and the z axis

normal to the surface. The height of the surface above the x–y plane will be denoted by h.[5]

Although the beam was focused, it remained slightly divergent. We exploited this fact in two different ways. First, because the beam was focused, moving away from the beam center in the y direction produces a reduction in the flux f and hence in the fluence F. By moving far enough away, the fluence could be reduced almost to zero. Secondly, because the beam was divergent, we were able to make detailed surveys of the patterns formed at a sequences of closely spaced angles of incidence by imaging at different locations along the x axis. We used this ability to identify the angles of incidence Θ at which the five different kinds of pattern are most clearly defined at the beam center. The range of Θ that could be accessed within a single sample exceeded 2.7° at normal incidence. This range decreases as Θ increases due to the limited lateral sample size.

It has been known for some time that unintended co-deposition of metal impurities can completely alter the patterns produced by ion bombardment of a silicon surface [9, 42–51]. We therefore took great care to ensure that impurities were not co-deposited during IBI. In particular, by targeting a point close to the center of the silicon sample with a focused beam, we made sure that virtually all of the incident ions struck the sample rather than the stainless steel sample holder or chamber walls. In addition, we placed a sacrificial portion of a silicon wafer over the part of the sample holder that could possibly have been exposed to the ion beam to prevent the sputter-deposition of the metallic species that make up the holder.

3. Experimental results

Figure 2 shows images of the patterns on the sample surface at the beam center following irradiation with the 2 keV Kr ion beam for selected values of Θ. We arranged for the fluence F to have the value 1950 ions nm^{-2} in each case by adjusting the irradiation time to compensate for the geometric factor $\cos\Theta$.

Parallel-mode ripples form for $\Theta = 74°$, as seen in figure 2(a). The topography is much richer than this simple, traditional description would suggest, however, since raised and depressed triangular regions are evident, and these are traversed by the ripples. The obliquely-oriented edges of the triangular nanostructures are marked in red and blue in figure 2(a′). The PSD of the surface height appears in the inset of figure 2(a). It displays an X-shaped structure centered on the origin in addition to the two peaks that arise from the parallel-mode ripple pattern. This 'X' in the PSD is an important signature of the triangular nanostructures. The angle subtended by the two legs of the X-shaped structure, $\phi \cong 46°$, matches the mean angle subtended by the beam-facing apex of the triangular structures well. (See the guidelines in figure 2(a) and its inset.) The length of the legs of the X-shaped structure in the PSD is an indication of the spread in the distances between the similarly oriented edges of neighboring triangular structures that are shown in red and blue in figure 2(a′).

Figure 3(a) shows the pattern at the same angle of incidence as figure 2(a), but this image was taken far from the origin on the y-axis and hence for a much reduced value of the fluence F. Only parallel-mode ripples are observed—the triangular nanostructures do not appear in the real space image of the surface, and the X-shaped structure is not present in the corresponding PSD. This observation shows that nonlinear effects contribute to the formation of the triangular structures in figure 2(a). The work of Loew and Bradley strongly suggests that linear dispersion is also an important factor in the formation of these nanostructures [39].

For $\Theta = 78°$, neither parallel- nor perpendicular-mode ripples are immediately apparent in figure 2(b), an AFM scan for the fluence $F = 1950$ ions nm^{-2}. Traditionally, this angle of incidence would be thought to be close to the angle of incidence Θ_r where the instability is biaxial and mounds form on the surface [7]. However, the real-space image for a much lower ion fluence and the same value of Θ that is shown in figure 3(b) establishes that the instability is in fact not biaxial, since parallel-mode ripples form at early times. This conclusion is supported by the corresponding PSD that appears in the inset of figure 3(b).

The surface topography for $\Theta = 78°$ and $F = 1950$ ions nm^{-2} is complex and has structure on a broad range of length scales, as seen in figures 2(b) and (b′). A histogram of the surface slope angle $\delta \equiv -\arctan(\partial h/\partial x)$ displays two peaks (see figure 4), which indicates that the surface does not consist of mounds but instead is terraced. The plot of $h_x \equiv \partial h/\partial x$ versus x and y shown in figure 5(a) confirms this, but also shows that the surface steps are not straight and so the terraces are irregular. In fact, a significant portion of the terrace edges are nearly parallel to two preferred diagonal directions. (See the guidelines in figure 2(b) and the edge-enhanced image in figure 5(a).) Some of the edges even form wedges with their apexes facing the ion beam. The mean angle subtended by the two edges of a wedge is ∼56°. The PSD shown in the inset of figure 2(b) also displays an X-shaped structure, albeit faintly. The value of ϕ determined from the 'X' in the PSD agrees well with the angle subtended by the two preferred directions in the real-space image. It is therefore likely that dispersion once again makes a significant contribution to the pattern formation. At the same time, the terraces present on the surface strongly suggest that the cubic nonlinearity h_x^3 also plays an important role at this angle of incidence [41, 52].

Figure 2(b′) is a magnified image of a region in figure 2(b). Careful examination of the terraces reveals that there are parallel-mode ripples on them. The parallel-mode ripples are most easily seen in the inset of figure 2(b′). This image was obtained by flattening the image of the region outlined by a dashed square in figure 2(b′). Parallel-mode ripples on terraces were previously reported for both silicon [53] and germanium [12] targets.

[5] Because the sputter yield depends on the local angle of incidence and the ion beam was divergent, the positions of maximal f and W could differ. However, a beam divergence of ±1.35° was estimated from the beam profile provided by the manufacturer of the ion gun. This small divergence could contribute to the uncertainty in the angle assigned to each pattern, but the uncertainty is certainly less than ±1.35°.

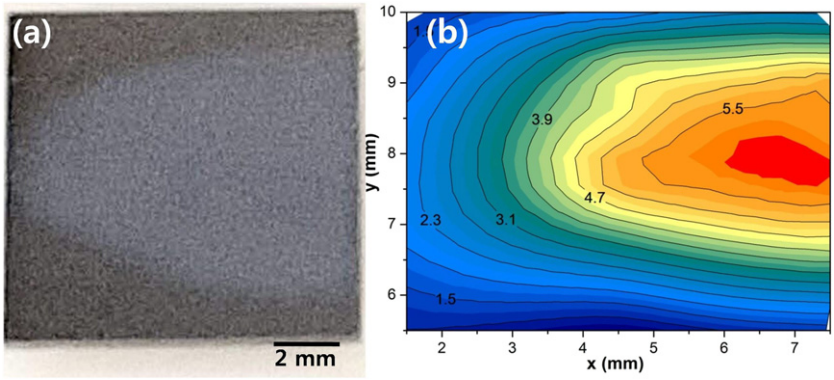

Figure 1. (a) A photographic image of the sample after irradiation with a 2 keV Kr ion beam with the angle of incidence $\Theta = 71^\circ$ for 600 min. The spatial variation of the reflectivity is an indication of the damage done to the surface and shows the beam cross-section at the Si surface. (b) Contour map of the surface width W of Si irradiated by a 2 keV Kr ion beam at $\Theta = 74^\circ$ for 143 min. The image was produced *ex situ* using an AFM in the non-contact mode.

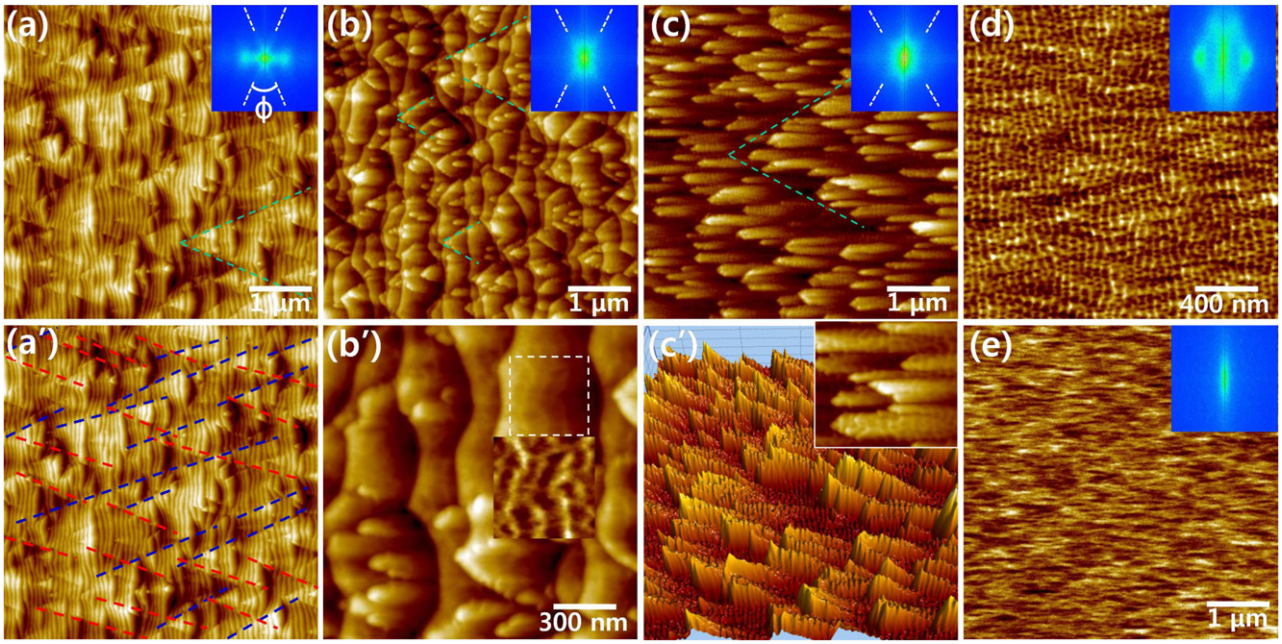

Figure 2. AFM images of representative patterns formed on the Si surface by irradiation with a 2 keV Kr ion beam for an angle of incidence Θ equal to (a) 74°, (b) 78°, (c) 80.5°, (d) 82°, and (e) 85°. In each case, the ion fluence (F) was 1950 ions nm^{-2} and the surface projection of the ion beam's direction points from left to right. The image sizes are 5 μm $\times$ 5 μm except (d), which is 2 μm $\times$ 2 μm. The inset in each image shows its power spectral density (PSD). (Unless otherwise noted, in these images and in all of the PSDs that follow, the PSD raised to the one-quarter power was actually plotted to show more detail.) (a′) The image shown in (a) with some of the obliquely-oriented edges of the triangular structures along the two preferred directions displayed in red and blue, respectively. The distances between the neighboring edges of the same orientation in adjacent triangular nanostructures have a broad distribution. This produces the legs of the X-shaped structure in the PSD shown in the inset of (a). (b′) A zoomed-in image of a portion of (b) reveals a parallel-mode ripple pattern on the terraces. The inset shows a flattened image of the dashed square region that makes the ripples on the terrace conspicuous. (c′) A perspective view of a region in (c) reveals that the fin structure is decorated by parallel-mode ripples. Inset: a magnified image of a region of (c) showing the parallel-mode ripple pattern on the surface.

For $\Theta = 80.5^\circ$ and the fluence $F = 1950$ ions nm^{-2}, the surface is no longer terraced. Instead, it is made up of truncated ridges or 'fins' running along the x direction, as shown in figure 2(c). The three-dimensional surface image in figure 2(c′) reveals that the fins have a face that faces the beam and a gradually descending ridge with sloped flanks. The ridges are narrow and the slope $h_y \equiv \partial h/\partial y$ changes quite rapidly across them. Similar structures were observed on ion-irradiated silicon surfaces by Macko *et al* [9].

The fin-shaped structures are not regularly spaced, and accordingly there is no discernible peak along the k_y axis in the PSD of the surface height—see the inset of figure 2(c). The pattern for $\Theta = 80.5^\circ$ should therefore not be described as a perpendicular-mode ripple, although that has been done

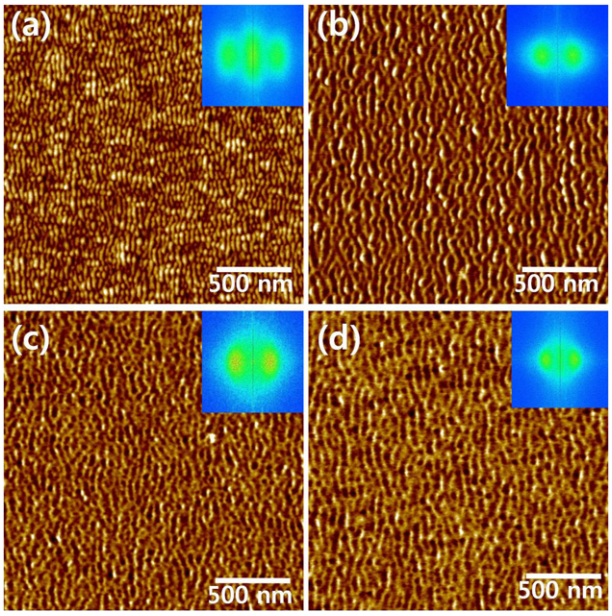

Figure 3. (a)–(d) AFM scans of the parallel-mode ripple patterns obtained at the same angles of incidence as figures 2(a)–(d), but for much lower fluences F. Each of the images is 2 μm $\times$ 2 μm. The insets are the PSDs of the real-space images.

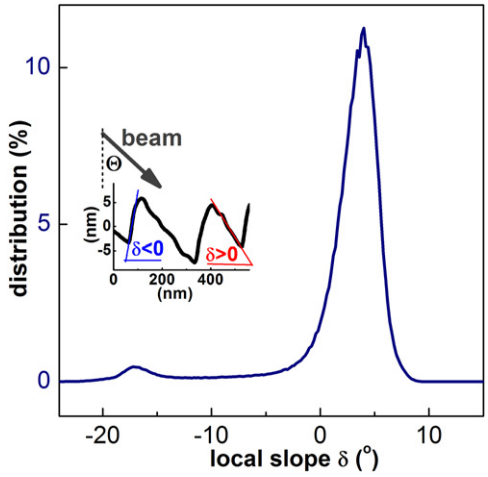

Figure 4. The distribution of the local slope angles δ is given for the pattern formed for the angle of incidence $\Theta = 78°$. Inset: the sign convention for δ is defined as depicted.

elsewhere [8–10]. In fact, parallel-mode ripples decorate the whole surface, as seen in figure 2(c′) and its inset as well as in figure 5(b). In addition, only parallel-mode ripples are present on the surface for low fluences, as shown by figure 3(c).

A faint 'X' is present in the PSD shown in figure 2(c). This suggests that dispersion may also play a role in the pattern formation for $\Theta = 80.5°$. Correspondingly, the ends of the fins are shaped and arranged like vees, as highlighted by the guidelines in the real-space image in figure 2(c). This is most apparent in the edge enhanced image in figure 5(b).

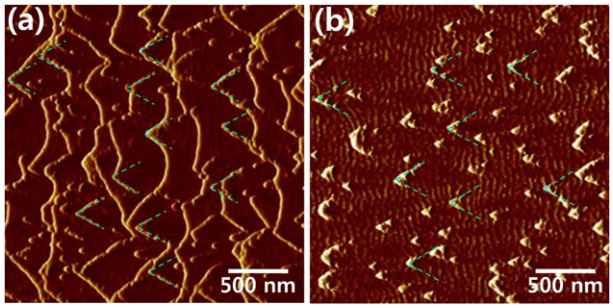

Figure 5. Edge-enhanced images showing h_x for a portion of (a) figure 2(b) and (b) figure 2(c). The wedges in the figures subtend angles that agree well with the angles ϕ determined from the X-shaped structures in the corresponding PSDs.

When Θ is increased to 82°, the fins are replaced by a parallel-mode ripples, as shown in figure 2(d). Interestingly, nanoholes are present between the ripple crests, giving the surface an appearance that is somewhat reminiscent of a mesh. (Note that in this case the image size was reduced to 2 μm $\times$ 2 μm so that details of the pattern could be seen clearly.) An analogous pattern has been observed on a Ge surface bombarded at a comparable high angle of incidence [12]. The PSD in the inset of figure 2(d) shows an X-shaped structure centered on the origin as well as two peaks coming from the parallel-mode ripple pattern. Once again, only parallel-mode ripples can be discerned for low fluences (see figure 3(c)).

To investigate the structure in the mesh pattern shown in figure 6(a), we smoothed the surface height to reduce the short-wavelength roughness produced by shot noise in the ion beam. A nanohole was defined to be a connected set of points that have positive surface curvatures in both the x- and y-directions. The nanoholes in figure 6(a) are shown in figure 6(b). The PSD of figure 6(b), which is shown in the inset, reproduces the structure seen in the PSD in figure 6(a) except in the vicinity of the origin at $k_x = k_y = 0$. In particular, the opening angles of the Xs in these two PSDs are nearly the same: $\phi \sim 38°$. This shows that the X-shaped structure in the inset of figure 6(a) comes from the arrangement of the nanoholes.

Our next step was to explore the order in the arrangement of nanoholes. We took the position of each nanohole to be its centroid position. These locations were then used to construct the corresponding two-dimensional Delaunay triangulation. This places a bond between each nearest-neighbor pair of nanoholes, as shown in figure 6(c). A histogram of the angles that the bonds in the Delaunay triangulation make with the x axis is shown in figure 6(d). There are peaks near $\pm 19°$ and $\pm 90°$. These peaks demonstrate that there is orientational order in the arrangement of nanoholes. The bond angles near $\pm 90°$ come from neighboring pairs of nanoholes with the bond that joins them approximately parallel to the y direction. These peaks in the bond angle distribution occur because the nanoholes have a tendency to be located in the troughs of the parallel-mode ripples. The two peaks of the bond angle distribution closer to the origin in figure 6(d) were fitted with Gaussians. The fits show that these peaks occur at the angles

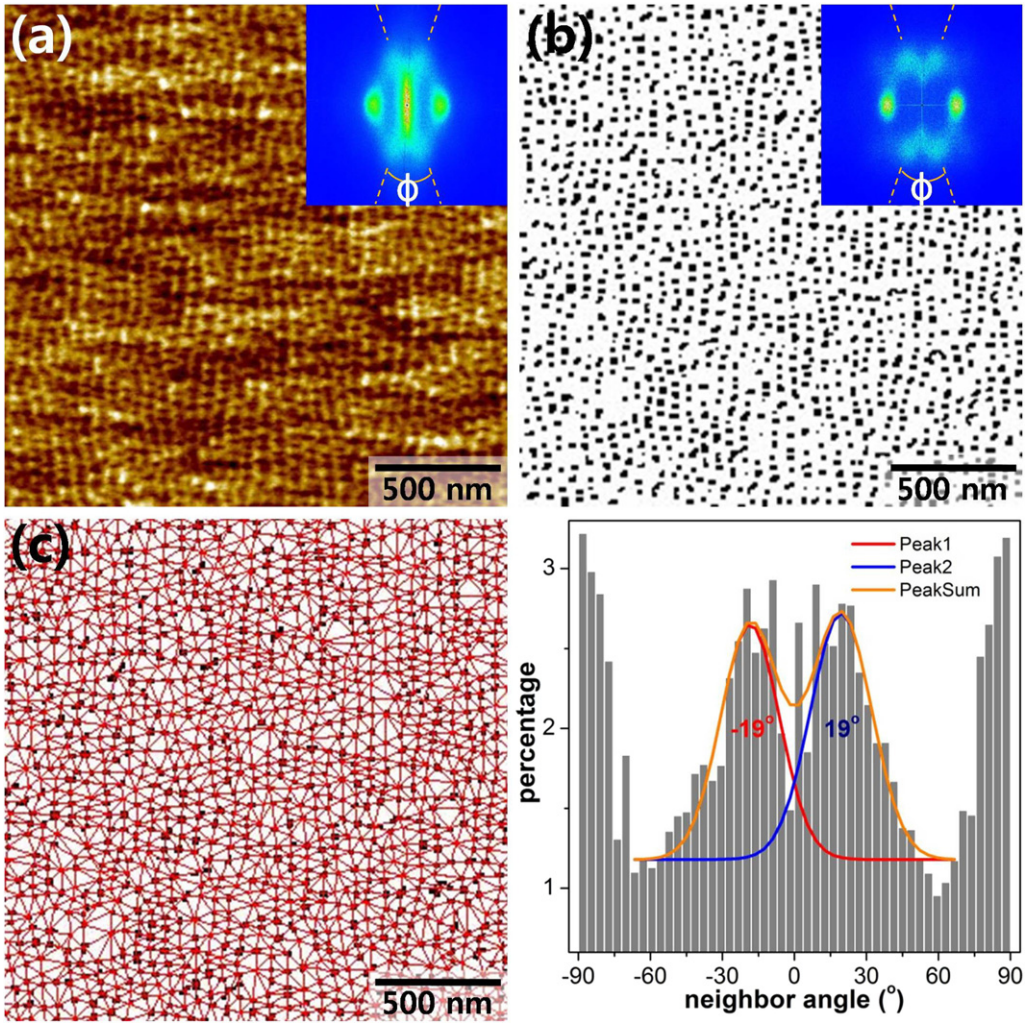

Figure 6. (a) A mesh pattern that formed for $\Theta = 82°$. The inset shows the corresponding PSD. (b) The nanoholes that make up the mesh pattern in panel (a) are displayed in black. The inset is the corresponding PSD. (c) The Delaunay triangulation of the nanohole positions in (b). The bonds connect nearest-neighbor pairs of holes. (d) Histogram of the angles that the bonds in the Delaunay triangulation make with the x axis.

$\pm 19°(\pm 2°)$. These angles coincide with the angles that the X in the PSD in figure 6(a) makes with the k_y axis. Thus, the X that is observed in the PSD of the mesh pattern is due to the orientational order of the nanoholes. The peaks in the histogram at $\pm 19°$ show that the nanoholes tend to be arranged in chains that are oblique to the projected ion direction.

For $\Theta = 85°$, the mesh-like pattern has disappeared. Instead, a so-called perpendicular-mode ripple pattern develops, as shown in figure 2(e). Patterns of this kind have been reported by numerous groups for both silicon [9–11] and germanium [13] targets. The PSD in the inset of figure 2(e), however, does not exhibit any peaks, as previously reported [17]. In addition, no peaks are present in the PSDs for lower fluences shown in figure 7. As a consequence, the surface morphology should *not* be described as a perpendicular-mode ripple pattern.

Our results show that when the angle of incidence is changed by just a few degrees, the topography of the surface can change dramatically. These changes are attended by a wide variation in the surface width W (the root-mean square deviation of the surface height from its average value), as seen in figure 8. As Θ is increased, W passes through a maximum value of 7.3 nm in the vicinity of 78° and declines to less than 4.1% of its maximum value for $\Theta = 85°$.

4. Comparison with theoretical models

In section 3, we discussed the different kinds of patterns that emerge as Θ is increased from 74° to 85°. In our comparison of these experimental results with theoretical models, however, it will be convenient to consider the five kinds of patterns formed in a different order. We will begin with the morphologies found for $\Theta = 74°$ and 80.5° since these patterns are best modeled by equations of motion that have already been studied, or by modifications of those models. The patterns that develop for $\Theta = 78°$ will be discussed next because they seem to be a complex hybrid of the patterns found for $\Theta = 74°$ and 80.5°. We will then advance a model for the noisy, streaked surfaces that form for $\Theta = 85°$. Finally, we will close this section

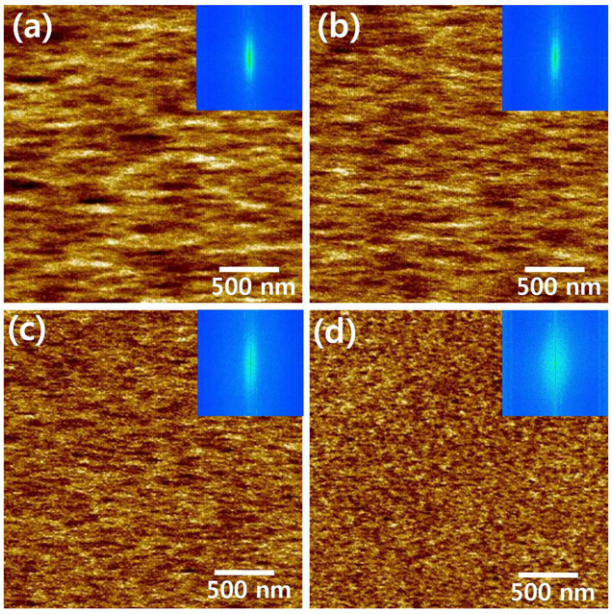

Figure 7. AFM images for $\Theta = 85^\circ$ obtained at points on y-axis away from the beam center at the origin. As we go from panels (a) to (d), the distance from the origin grows larger and the corresponding fluence F grows smaller. The farther from the origin, the fainter the so-called perpendicular-mode ripple pattern becomes. In panel (d), no ripple pattern is recognizable.

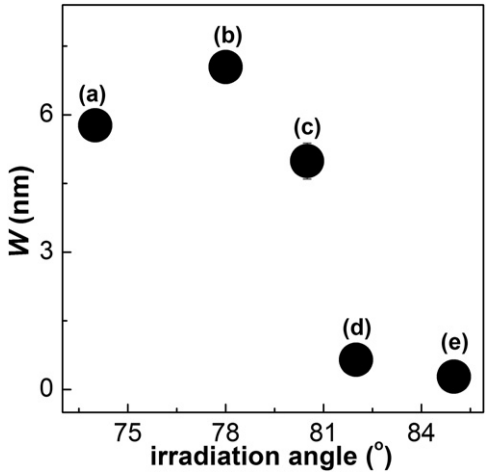

Figure 8. The surface width W plotted versus the ion irradiation angle Θ for the fluence $F = 1950$ ions nm^{-2}. The labels (a) to (e) in the figure indicate the values of W for figures 2(a)–(e). Most of the error bars are smaller than the symbol size.

with a brief discussion of the mesh-like pattern that is found for $\Theta = 82^\circ$. In this case, no plausible model is known at the present time.

The most widely employed model of pattern formation on the surface of solid that is bombarded with an obliquely-incident ion beam is the AKS equation. However, for angles of incidence Θ in excess of the threshold angle for pattern formation $\Theta_{\rm th}$ but close to it, linear dispersion has been shown to have an important effect on the pattern formation [54]. Such a term does not appear in the AKS equation. Simulations carried out by Loew and Bradley have shown that once a linearly dispersive term has been appended to the AKS equation, raised and depressed triangular regions traversed by parallel-mode ripples can emerge as time passes [39]. These triangular nanostructures are similar to the ones present in figure 2(a), but their edges are less distinct. Moreover, the PSDs of patterns generated by the EOM studied by Loew and Bradley have a much weaker X-shaped structure than the one that appears in the experimental PSD shown in the inset of figure 2(a).

The conserved Kuramoto–Sivashinsky (CKS) nonlinearity produces ripple coarsening [55, 56], a phenomenon that is frequently observed in experiments [5, 57]. This term is also needed if the pattern formation that occurs on a silicon target that is rocked during ion bombardment is to be reproduced [58]. Although the effect of the CKS term is negligible near the threshold angle for pattern formation [54], the angle of incidence Θ in the case of figure 2(a) was 74° and so was significantly larger than $\Theta_{\rm th} \sim 55^\circ$. The CKS term may therefore have played an important role in the dynamics. Adding such a term to Loew and Bradley's EOM yields

$$h_t = -A_1 h_{xx} + A_2 h_{yy} - B\nabla^2\nabla^2 h + \lambda_1 h_x^2 + \lambda_2 h_y^2 + \alpha h_{xxx} + \beta h_{xyy} + (\partial_x^2 + r\partial_y^2)(\mu_1 h_x^2 + \mu_2 h_y^2). \quad (1)$$

Here $h = h(x, y, t)$ is the height of the solid surface above the point with coordinates x and y in the x–y plane at time t, as measured in a suitably chosen moving frame of reference. The subscripts x, y and t on h denote partial derivatives with respect to these variables. A_1, A_2, B, λ_1, λ_2, α, β, r, μ_1 and μ_2 are constants that depend on Θ. For $\mu_1 = \mu_2 = 0$, no CKS term is present and (1) reduces to the EOM studied by Loew and Bradley. When, in addition, α and β are both zero, linear dispersion is absent and (1) becomes the AKS equation. Finally, we note that the most general form of (1) is a special case of the EOM for an ion-irradiated solid surface that results from a 'hydrodynamic' model in which a layer near the surface of the solid is mobilized by the impinging ions [55, 56].

We carried out numerical integrations of (1) with low amplitude spatial white noise initial conditions for selected parameter values. Periodic boundary conditions were employed. A nonzero value of μ_1 was chosen so that a nontrivial CKS term appears in the EOM. The results are shown in figure 9. Triangular nanostructures are evident for α equal to 1, 5 and 10. In addition, the corresponding PSDs display a prominent X-shaped structure centered on the origin, just as in the experimental PSD shown in the inset in figure 2(a). The apex opening angle of the triangular nanostructures ϕ is a decreasing function of α. For $\alpha = 50$, the opening angle is small enough that the triangular nanostructures evident for smaller α values have been reduced to streaks.

The triangular nanostructures appear briefly for a time after the linear regime in simulations of Loew and Bradley's EOM but soon disappear: see figures 10(a)–(a″). In contrast, the triangular structures persist for a much longer time interval and get larger with the passage of time if the coefficient μ_1 in (1) is nonzero, as shown in figures 10(b)–(b″). Triangular nanostructures are found for a broad range of ion fluences and increase in size as the fluence increases in our experiments, as seen

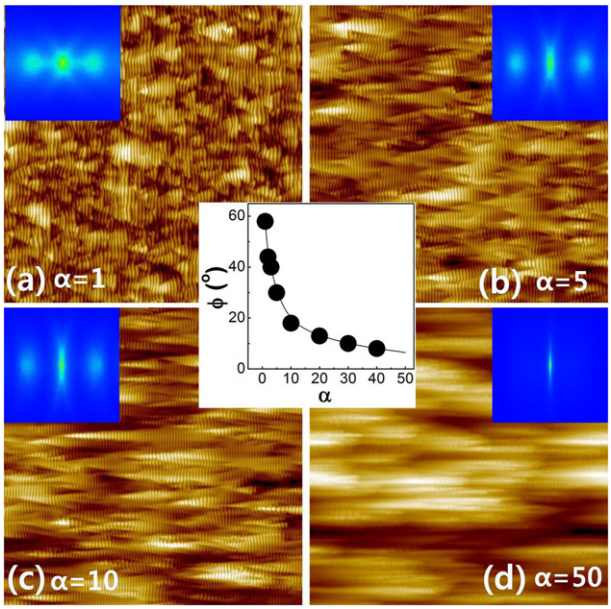

Figure 9. Real space images obtained by numerical integration of (1) with the coefficient α set equal to (a) 1, (b) 5, (c) 10, and (d) 50 at time $t = 100$. The values of the other coefficients in (1) were $A_1 = A_2 = B = 1$, $\lambda_1 = 0.5$, $\lambda_2 = \beta = 0$, $r = 1$, $\mu_1 = -0.25$, and $\mu_2 = 0$. The spatial grid spacing was $\Delta x = 1$, the time step was $\Delta t = 0.0001$ and the domain size was 1024×1024. Only a quarter of the full simulated images is shown to make the details of the patterns more readily apparent. The inset of each image is the corresponding PSD. The center plot shows the apex opening angle of the triangular nanostructures ϕ versus α.

figures 10(c)–(c″). This provides additional evidence that the CKS term significantly influences the dynamics for the angle of incidence $\Theta = 74°$.

The experimental surface pattern shown in figure 2(c) has many features in common with surfaces produced by simulations of the HPB equation

$$h_t = -A_1 h_{xx} + A_2 h_{yy} - B\nabla^2\nabla^2 h + \lambda_1 h_x^2 + \lambda_2 h_y^2 + a h_x^3 + b h_x h_y^2. \quad (2)$$

The terms proportional to h_x^2 and h_y^2 in this equation result from expanding the slope dependence of the sputter yield to second order in the surface gradient [16, 59]. Similarly, the terms proportional to h_x^3 and $h_x h_y^2$ appear if terms up to third order in h_x and h_y are retained in this expansion [40, 41]. For $a = b = 0$, the HPB equation (2) reduces to the AKS equation. Just as the terms proportional to h_{xxx} and h_{xyy} in (1) do, the cubic nonlinearities in the HPB equation (2) break the symmetry under the transformation $x \to -x$ that the AKS equation possesses even though the experimental setup does not.

The results of a simulation of the HPB equation with a low amplitude spatial white initial condition are shown in figure 11. For the chosen parameter values, parallel-mode ripples appear at early times, as shown in figure 11(a). Fins develop at longer times and grow larger as time passes, as seen in figures 11(b) and (c). Each fin has a sloped facet facing the beam as well as sloped facets that flank its gradually descending central ridge. The enlargement of a portion of the fins in figure 11(c) that is shown in figure 11(c′) clearly shows that ripples are present on the fins. The simulated surfaces therefore resemble the AFM images we obtained for $\Theta = 80.5°$ in a number of key respects. The experimental surfaces do not have well-defined facets, however.

As we saw in section 3, at high fluences, the distribution of surface slope angles is bimodal and the surface is terraced for $\Theta = 78°$. In addition, parallel-mode ripples are evident at early times and also on the terraces at longer times. The HPB model does yield surfaces with these characteristics for a range of parameter values, as illustrated by figure 12. The model fails to reproduce the very complicated surface structure seen in the experiments in the high fluence regime, however. This may be because the HPB equation includes neither linear dispersive terms nor the CKS nonlinearity, and, as we have seen, these terms play an important role in the dynamics for the somewhat smaller angle of incidence $\Theta = 74°$.

As we have discussed, the pattern obtained for $\Theta = 85°$ shown in figure 2(e) should not be described as perpendicular-mode ripples. The corresponding PSD has a central maximum but does not have peaks on either the k_x or k_y axes. This is also true for lower ion fluences, as seen in figure 7. These results strongly suggest that the surface is stable for $\Theta = 85°$. The surface, however, does not remain flat when ion bombardment begins because there is shot noise in the incident ion flux. As a first approximation, the effects of shot noise are negligible for the smaller angles of incidence we studied. For $\Theta = 85°$, however, the root-mean square surface width is quite small (see figure 8) and so the effects of noise are more important in this case. Including the effect of shot noise, the AKS equation is

$$h_t = \nu_1 h_{xx} + \nu_2 h_{yy} - B\nabla^2\nabla^2 h + \lambda_1 h_x^2 + \lambda_2 h_y^2 + \eta, \quad (3)$$

where ν_1 and ν_2 are both positive if the surface is stable and $\eta = \eta(x, y, t)$ is uncorrelated Gaussian white noise with zero mean and a variance proportional to the ion flux [16, 59]. The term $-B\nabla^2\nabla^2 h$ can be omitted from (3) because long wavelength disturbances are strongly suppressed by the smoothing effect of the terms $\nu_1 h_{xx}$ and $\nu_2 h_{yy}$. If, in addition, the effect of noise is relatively weak, the amplitude of the surface disturbance will remain small and the nonlinear terms may be omitted from (3), yielding

$$h_t = \nu_1 h_{xx} + \nu_2 h_{yy} + \eta. \quad (4)$$

Equation (4) is an anisotropic version of the Edwards–Wilkinson equation [60].

Atomistic simulations combined with the crater function formalism show that for 1 keV Ar ion bombardment of a silicon target, the coefficient of h_{xx} in the EOM can change sign from negative to positive and then increase rapidly as Θ nears 90° [61]. We therefore took ν_1 to be substantially larger than ν_2: for the sake of illustration, we adopted the values $\nu_1 = 1$, $\nu_2 = 0.01$ and took the noise amplitude to be 0.1. The results of integrating (4) numerically with these parameter values are shown in figure 13. The surface is quite noisy, but there are 'streaks' that are elongated in the x direction, much as in the AFM image shown in figure 2(e). These streaks arise because ν_1 was chosen to be significantly larger than ν_2.

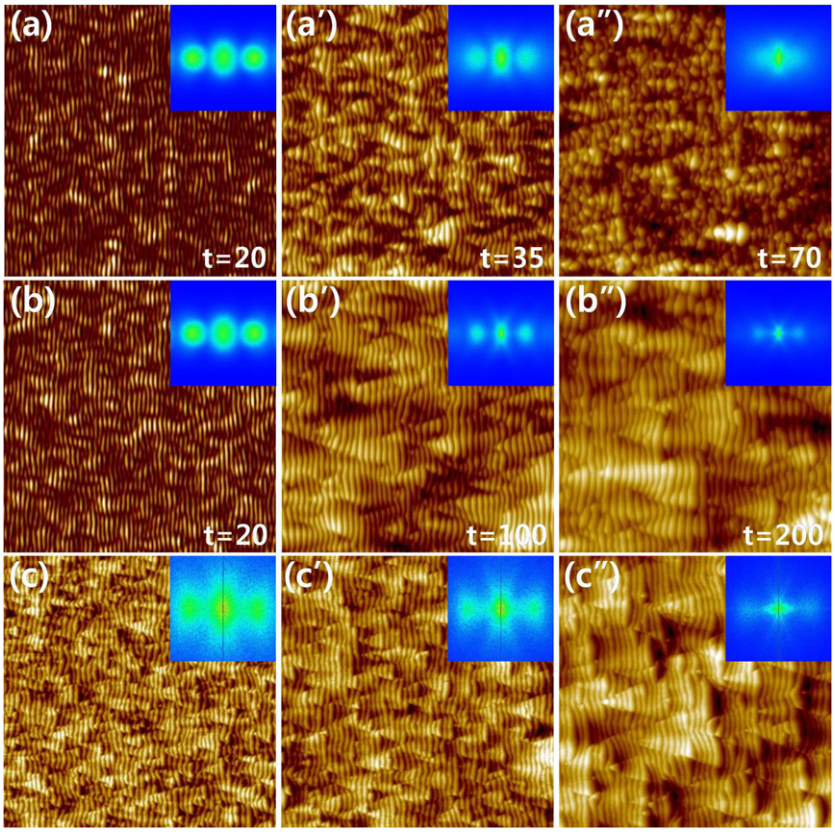

Figure 10. Panels (a)–(a″) and (b)–(b″): real space images obtained by numerical integration of (1) with the coefficients $A_1 = A_2 = B = 1$, $\lambda_1 = 0.5$, $\lambda_2 = \beta = 0$ and $\alpha = 2$. The insets are the corresponding PSDs. Panels (a)–(a″) show the surface for $\mu_1 = \mu_2 = 0$ at simulation times 10, 35, and 70, respectively. Triangular structures are present within a very limited time interval around $t = 35$ and the corresponding PSD displays only a weak X-shaped structure. Panels (b)–(b″) show the surface for $\mu_1 = -0.25$ and $r = \mu_2 = 0$ at simulation times 10, 100, and 200, respectively. The triangular structures are much more sharply defined, persist over a much longer time interval than for $\mu_1 = \mu_2 = 0$, and grow larger with the passage of time. The X-shaped structures in the PSDs in (b′) and (b″) are also much more readily apparent than the one in panel (a′). The spatial grid spacing was $\Delta x = 1$, the time step was $\Delta t = 0.0001$, and the domain size was 512×512. Panels (c)–(c″) show experimental AFM surface scans for $\Theta = 74^\circ$ with the ion fluence increasing from left to right. These images are 3 μm on a side. The images were taken at three points on the y-axis that were successively closer to the origin. The ion fluence could not be quantified, since the detailed functional dependence of the ion flux on y is not known.

The relatively small value of ν_2 means that smoothing in the y direction is weak, and consequently shot noise must be taken into account. There are no peaks away from the origin in the PSD shown in figure 13(b) and the central peak is elongated in the k_y direction, just as in the inset of figure 2(e). The model therefore produces results consistent with our experiments. A detailed comparison between the theory and the experiments would require precise values for the parameters in (4), however.

The genesis of the pattern in figure 2(d) is a puzzle and an interesting topic for future study. The X-shaped structure that passes through the origin in the PSD suggests that dispersion and the CKS nonlinearity play important roles in the pattern formation, just as they do in the case of figure 2(a). There is no evidence of terracing or fin formation, which indicates that if cubic nonlinearities are present in the EOM, their coefficients are small. We might therefore conclude that the EOM (1) is an appropriate model of the surface dynamics. However, at least for the choices of parameter values we have investigated, (1) does not produce mesh-like topographies that resemble figure 2(d). It is possible that if additional terms were included in (1), the resulting EOM would generate a mesh-like pattern for a range of parameter values. It is unclear at the present time just what those additional terms should be, or whether the models considered to date omit some essential physics.

5. Comparison with previous experimental work

As we mentioned in the introduction, the nanoscale patterns that develop on the (100) surface of silicon when it is irradiated with a 2 keV Kr ion beam have been studied in the past by Macko *et al* [9] and Engler *et al* [37]. Our work complements and extends those studies.

There are of course numerous studies of the patterns produced by bombardment of silicon targets with ions of various species and energies. (See references [5, 37] for reviews.) In this section, we will confine ourselves to comparing the results

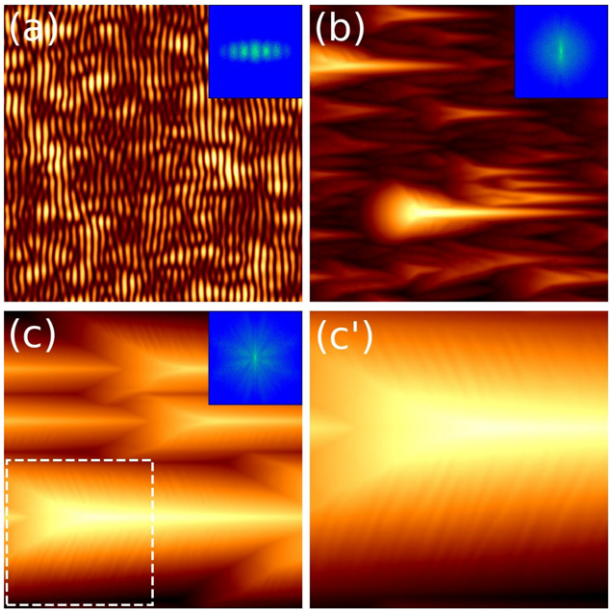

Figure 11. Real space images with PSD insets obtained by a numerical integration of (2) at times (a) $t = 40$, (b) $t = 300$, and (c) $t = 1000$. The image in panel (c′) is a magnified view of the region outlined with dashed lines in panel (c). The PSD insets are plotted on a logarithmic color scale to show more detail. The values of the coefficients in (2) were $A_1 = 1$, $A_2 = -0.3$, $B = 1$, $\lambda_1 = 5$, $\lambda_2 = 0.5$, $a = 1$, and $b = 3$. The spatial domain in panels (a)–(c) has a side length of 120π and 512×512 grid points. The time step was $\Delta t = 0.0025$.

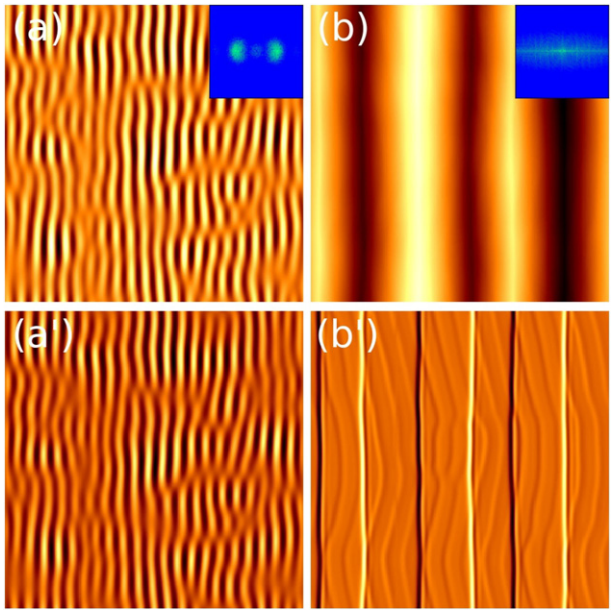

Figure 12. Real space images with PSD insets obtained by a numerical integration of (2) at times (a) $t = 40$ and (b) $t = 1000$. The images in panels (a′) and (b′) show the curvature h_{xx}. The PSD insets are plotted on a logarithmic color scale. The values of the coefficients in (2) were $A_1 = 1$, $A_2 = -0.4$, $B = 1$, $\lambda_1 = 0.05$, $\lambda_2 = 1$, $a = 1$, and $b = 0$. The spatial domain in each panel has a side length of 60π and 256×256 grid points. The time step was $\Delta t = 0.0025$.

of our experimental work to past studies of the irradiation of silicon with a 2 keV krypton ion beam.

The most detailed study of the 2 keV Kr^+–Si ion-target combination that appeared prior to our work is that of Engler *et al* [37]. Engler *et al* concluded that patterns form on the silicon surface for angles of incidence Θ between 58° and 79°, and that for Θ outside this interval, the surface remains flat. We, however, found that a mesh pattern is formed for $\Theta = 82°$. Experiments for this value of Θ were not carried out by Engler *et al*, and, as a result, they did not observe this fascinating type of pattern formation. In addition, we found that for $\Theta = 80.5°$, the surface does not remain flat, contrary to the assertion of Engler *et al*. Instead, fins develop. This type of topography was not reported in Engler *et al*'s paper, although a somewhat similar morphology appears in Macko *et al* [9] for $\Theta = 79°$.

Engler *et al* found that parallel-mode ripples form for $58° \leqslant \Theta \leqslant 63°$ and that terraced surfaces develop for $67° \leqslant \Theta \leqslant 79°$ and high ion fluences. For $\Theta = 78°$, we found that a complex terraced surface forms, and that this surface morphology closely resembles the one observed by Engler *et al* for $\Theta = 75°$. In contrast, for $\Theta = 74°$, we observed the formation of triangular nanostructures traversed by parallel-mode ripples rather than terraces. It is possible that terraces would have emerged had we continued bombarding the surface to the highest fluence studied by Engler *et al*, which was more than twice our highest fluence.

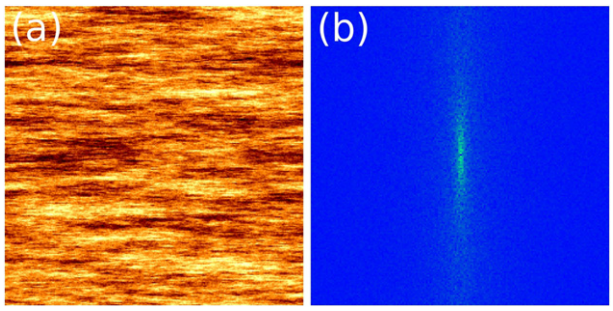

Figure 13. A real space image (a) and its PSD (b) at time $t = 1000$ obtained by numerical integration of (4). The values of the coefficients in (4) were $\nu_1 = 1$ and $\nu_2 = 0.01$, and the amplitude of the noise term η was 0.1. The spatial domain in panel (a) has a side length of 60π and 256×256 grid points. The time step was $\Delta t = 0.1$.

It is interesting to note that triangular nanostructures traversed by parallel-mode ripples appear to have formed in the experiments of Engler *et al* with $\Theta = 63°$, although it is difficult to be certain because the dimensions of their images are a factor of five smaller than ours. Engler *et al*, however, claimed that the parallel-mode ripples they observed were traversed by disordered perpendicular-mode ripples.

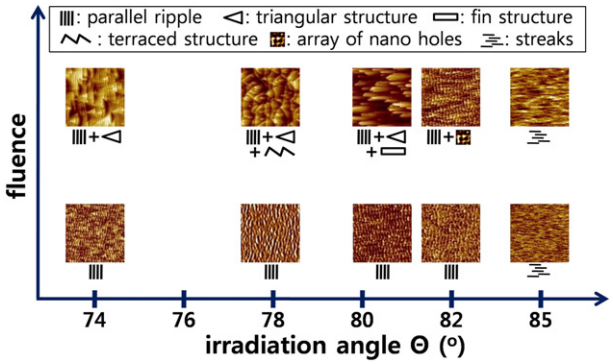

Figure 14. A 'phase diagram' which shows the patterns we observed for selected incidence angles Θ and fluences F. The schematic diagram shown beneath each AFM image summarizes the structural elements that combine to give the observed morphologies. For further details, see the main text.

6. Conclusions

In this paper, we studied the nanoscale patterns that develop on the (100) surface of silicon when it is irradiated with a broad 2 keV krypton ion beam. The results of our investigations are summarized by the 'phase diagram' given in figure 14, which shows the patterns we observed for selected incidence angles Θ and fluences F. In the span of only 11°, a total of five markedly different morphologies occur for high ion fluences. In contrast, for low fluences, only parallel-mode ripples are present for Θ equal to 74°, 78°, 80.5° and 82°. For $\Theta = 85°$, the solid surface appears to be stable, and to roughen only as a result of shot noise in the ion beam.

We have been able to reproduce some of the experimentally-observed patterns in simulations. Triangular nanostructures that closely resemble those found in our experiments for $\Theta = 74°$ form if a CKS nonlinearity is appended to the EOM proposed by Loew and Bradley [39]. This nonlinearity is known to produce ripple coarsening, as observed in many experiments [55, 56]. Our results once again highlight the importance of this term. Fins traversed by parallel-mode ripples are observed for $\Theta = 80.5°$. They also emerge in our simulations of the HPB equation [41] for a range of parameter values, which shows that the cubic nonlinearities that result from expanding the sputter yield to third order in the surface slope must be included in the EOM in this case. Finally, simulations of an anisotropic version of the Edwards–Wilkinson equation yield disordered surfaces with 'streaks' aligned with the projected ion direction, much like the surfaces in our experiments with $\Theta = 85°$.

For $\Theta = 78°$ and high ion fluences, the surface topography is complex and has structure on a broad range of length scales. At long length scales, the surface is terraced, but the parts of the terrace edges are wedge-shaped. The terraces are also decorated by short-wavelength, low amplitude parallel-mode ripples. The mesh-like pattern observed for $\Theta = 82°$ can be thought of as a parallel-mode ripple pattern with nanoholes in the troughs. The arrangement of nanoholes displays a degree of orientational order: in particular, the nanoholes tend to be arranged in chains along two directions that are oblique to the projected ion direction. So far as we have been able to determine, these two kinds of patterns are not reproduced by simulations of any of the equations of motion discussed in this paper. Explaining them remains a challenge for future theoretical work.

Acknowledgments

This work was supported by the Korean Research Foundation (NRF-2019R1F1A1040955) and by Grants DMS-1814941 and DMR-2116753 awarded by the U.S. National Science Foundation.

Data availability statement

All data that support the findings of this study are included within the article (and any supplementary files).

ORCID iDs

R M Bradley https://orcid.org/0000-0001-6233-9016
J-S Kim https://orcid.org/0000-0002-9286-7837

References

[1] Valbusa U, Boragno C and Buatier de Mongeot F 2002 Nanostructuring surfaces by ion sputtering *J. Phys.: Condens. Matter* **14** 8153
[2] Chan W L and Chason E 2007 Making waves: kinetic processes controlling surface evolution during low energy ion sputtering *J. Appl. Phys.* **101** 121301
[3] Cuerno R, Vázquez L, Gago R and Castro M 2009 Surface nanopatterns induced by ion-beam sputtering *J. Phys.: Condens. Matter* **21** 220301
[4] Cuerno R and Kim J-S 2020 A perspective on nanoscale pattern formation at surfaces by ion-beam irradiation *J. Appl. Phys.* **128** 180902
[5] Muñoz-García J, Vázquez L, Castro M, Gago R, Redondo-Cubero A, Moreno-Barrado A and Cuerno R 2014 Self-organized nanopatterning of silicon surfaces by ion beam sputtering *Mater. Sci. Eng.* R **86** 1–44
[6] Norris S A and Aziz M J 2019 Ion-induced nanopatterning of silicon: toward a predictive model *Appl. Phys. Rev.* **6** 011311
[7] Bradley R M and Harper J M E 1988 Theory of ripple topography induced by ion bombardment *J. Vac. Sci. Technol.* A **6** 2390
[8] Zhang K, Hofsäss H, Rotter F, Uhrmacher M, Ronning C and Krauser J 2009 Morphology of Si surfaces sputter-eroded by low-energy Xe-ions at glancing incident angle *Surf. Coat. Technol.* **203** 2395
[9] Macko S, Frost F, Ziberi B, Förster D F and Michely T 2010 Is keV ion-induced pattern formation on Si(001) caused by metal impurities? *Nanotechnology* **21** 085301
[10] Madi C S and Aziz M J 2012 Multiple scattering causes the low energy-low angle constant wavelength topographical instability of argon ion bombarded silicon surfaces *Appl. Surf. Sci.* **258** 4112
[11] Lopez-Cazalilla A *et al* 2018 Pattern formation on ion-irradiated Si surface at energies where sputtering is negligible *J. Appl. Phys.* **123** 235108

[12] Teichmann M, Lorbeer J, Ziberi B, Frost F and Rauschenbach B 2013 Pattern formation on Ge by low energy ion beam erosion *New J. Phys.* **15** 103029

[13] Datta D P, Garg S K, Basu T, Satpati B, Hofsäss H, Kanjilal D and Som T 2016 Temporal evolution of Ge surface topography under keV ion irradiation: combined effects of curvature-dependent sputter erosion and atomic redistribution *Appl. Surf. Sci.* **360** 131

[14] Chowdhury D and Ghose D 2017 Fabrication of nanoscale topographies on Ge(100) surface by low energy Ar^+ ion sputtering *Nucl. Instrum. Methods Phys. Res.* B **409** 197

[15] Metya A and Ghose D 2013 Investigation of ion beam induced nanopattern formation near the threshold energy *Appl. Phys. Lett.* **103** 161602

[16] Cuerno R and Barabási A-L 1995 Dynamic scaling of ion-sputtered surfaces *Phys. Rev. Lett.* **74** 4746

[17] Vivo E, Nicoli M, Engler M, Michely T, Vázquez L and Cuerno R 2012 Strong anisotropy in surface kinetic roughening: analysis and experiments *Phys. Rev.* B **86** 245427

[18] Carter G, Nobes M J, Paton F, Williams J S and Whitton J L 1977 *Radiat. Eff.* **33** 65

[19] Keller A, Roßbach S, Facsko S and Möller W 2008 Simultaneous formation of two ripple modes on ion sputtered silicon *Nanotechnology* **19** 135303

[20] Keller A, Facsko S and Möller W 2008 Minimization of topological defects in ion-induced ripple patterns on silicon *New J. Phys.* **10** 063004

[21] Castro M, Gago R, Vázquez L, Muñoz-García J and Cuerno R 2012 Stress-induced solid flow drives surface nanopatterning of silicon by ion-beam irradiation *Phys. Rev.* B **86** 214107

[22] Metya A, Ghose D, Mollick S A and Majumdar A 2012 Nanopatterning of mica surface under low energy ion beam sputtering *J. Appl. Phys.* **111** 074306

[23] Chowdhury D and Ghose D 2013 High fluence effect on Si ripple morphology developed by low energy ion beam sputtering *AIP Conf. Proc.* **1536** 353–4

[24] Teichmann M, Lorbeer J, Frost F and Rauschenbach B 2014 Ripple coarsening on ion beam-eroded surfaces *Nanoscale Res. Lett.* **9** 439

[25] Chowdhury D and Ghose D 2016 Tuning of nanopatterns on Si (100) substrate: role of ion beam processing parameters during sputtering *Adv. Sci. Lett.* **22** 105–10

[26] Gago R, Jaafar M and Palomares F J 2018 Surface morphology of molybdenum silicide films upon low-energy ion beam sputtering *J. Phys.: Condens. Matter* **30** 264003

[27] Hans S and Ranjan M 2021 Emergence of triangular features on ion irradiated silicon (100) surface *Surf. Sci.* **715** 121951

[28] Hauffe W 1976 Faceting mechanism in the sputtering process *Phys. Status Solidi a* **35** K93

[29] Flamm D, Frost F and Hirsch D 2001 Evolution of surface topography of fused silica by ion beam sputtering *Appl. Surf. Sci.* **179** 95

[30] Datta D P and Chini T K 2004 Atomic force microscopy study of 60 keV Ar-ion-induced ripple patterns on Si(100) *Phys. Rev.* B **69** 235313

[31] Karmakar P and Ghose D 2005 Nanoscale periodic and faceted structures formation on Si(1 0 0) by oblique angle oxygen ion sputtering *Nucl. Instrum. Methods* B **230** 539

[32] Adams D P, Mayer T M, Vasile M J and Archuleta K 2006 Effects of evolving surface morphology on yield during focused ion beam milling of carbon *Appl. Surf. Sci.* **252** 2432

[33] Wei Q, Lian J, Boatner L A, Wang L M and Ewing R C 2009 Propagation of ripples on pyrochlore induced by ion beam bombardment *Phys. Rev.* B **80** 085413

[34] Mishra P and Ghose D 2009 Effect of initial target surface roughness on the evolution of ripple topography induced by oxygen sputtering of al films *J. Appl. Phys.* **105** 014304

[35] Völlner J, Ziberi B, Frost F and Rauschenbach B 2011 Topography evolution mechanism on fused silica during low-energy ion beam sputtering *J. Appl. Phys.* **109** 043501

[36] Basu T, Datta D P and Som T 2013 Transition from ripples to faceted structures under low-energy argon ion bombardment of silicon: understanding the role of shadowing and sputtering *Nanoscale Res. Lett.* **8** 289

[37] Engler M, Macko S, Frost F and Michely T 2014 Evolution of ion beam induced patterns on Si(001) *Phys. Rev.* B **89** 245412

[38] Perkinson J C, Swenson J M, DeMasi A, Wagenbach C, Ludwig K F Jr, Norris S A and Aziz M J 2018 Sawtooth structure formation under nonlinear-regime ion bombardment *J. Phys.: Condens. Matter* **30** 294004

[39] Loew K M and Bradley R M 2019 Effect of dispersion on the nanoscale patterns produced by ion sputtering *Phys. Rev.* E **100** 012801

[40] Pearson D A and Bradley R M 2015 Theory of terraced topographies produced by oblique-incidence ion bombardment of solid surfaces *J. Phys.: Condens. Matter* **27** 015010

[41] Harrison M P, Pearson D A and Bradley R M 2017 Emergence and detailed structure of terraced surfaces produced by oblique-incidence ion sputtering *Phys. Rev.* E **96** 032804

[42] Ozaydin G, Özcan A S, Wang Y, Ludwig K F, Zhou H, Headrick R L and Siddons D P 2005 Real-time x-ray studies of Mo-seeded Si nanodot formation during ion bombardment *Appl. Phys. Lett.* **87** 163104

[43] Ozaydin G, Ludwig K F, Zhou H and Headrick R L 2008 Effects of Mo seeding on the formation of Si nanodots during low-energy ion bombardment *J. Vac. Sci. Technol.* B **26** 551

[44] Hofsäss H and Zhang K 2008 Surfactant sputtering *Appl. Phys.* A **92** 517

[45] Bradley R M 2011 Theory of nanodot and sputter cone arrays produced by ion sputtering with concurrent deposition of impurities *Phys. Rev.* B **83** 195410

[46] Cornejo M, Ziberi B, Meinecke C, Hirsch D, Gerlach J W, Höche T, Frost F and Rauschenbach B 2011 Self-organized patterning on Si(001) by ion sputtering with simultaneous metal incorporation *Appl. Phys.* A **102** 593

[47] Zhang K, Brötzmann M and Hofsäss H 2011 Surfactant-driven self-organized surface patterns by ion beam erosion *New J. Phys.* **13** 013033

[48] Bradley R M 2012 Producing ripple topographies by ion bombardment with codeposition of impurities: a curvature-dependent sputter yield is not required *Phys. Rev.* B **85** 115419

[49] Bradley R M 2013 Nanoscale patterns produced by ion erosion of a solid with codeposition of impurities: the crucial effect of compound formation *Phys. Rev.* B **87** 205408

[50] Bradley R M 2016 Morphological transitions in nanoscale patterns produced by concurrent ion sputtering and impurity co-deposition *J. Appl. Phys.* **119** 134305

[51] Moon B, Yoo S, Kim J-S, Kang S J, Muñoz-García J and Cuerno R 2016 Ion-beam nanopatterning of silicon surfaces under codeposition of non-silicide-forming impurities *Phys. Rev.* B **93** 115430

[52] Pearson D A, Bradley RM, Motta F C and Shipman P D 2015 Producing nanodot arrays with improved hexagonal order by patterning surfaces before ion sputtering *Phys. Rev.* E **92** 062401

[53] Engler M *et al* 2014 Silicide induced ion beam patterning of Si(001) *Nanotechnology* **25** 115303

[54] Bradley R M 2020 Theory of nanoscale ripple topographies produced by ion bombardment near the threshold for pattern formation *Phys. Rev.* E **102** 012807

[55] Muñoz-García J, Castro M and Cuerno R 2006 Nonlinear ripple dynamics on amorphous surfaces patterned by ion beam sputtering *Phys. Rev. Lett.* **96** 086101

[56] Muñoz-García J, Cuerno R and Castro M 2008 Coupling of morphology to surface transport in ion-beam irradiated surfaces: oblique incidence *Phys. Rev.* B **78** 205408
[57] Kim T C *et al* 2004 Kinetic roughening of ion-sputtered Pd(001) surface: beyond the Kuramoto–Sivashinsky model *Phys. Rev. Lett.* **92** 246104
[58] Jo S, Jun J, Lee E, Yoon S M, Seo J, Muñoz-García J, Cuerno R and Kim J-S 2020 Order improvement of surface nanopatterns via substrate rocking under ion bombardment: experiments and nonlinear models *Phys. Rev.* B **102** 045421
[59] Makeev M A, Cuerno R and Barabási A L 2002 Morphology of ion-sputtered surfaces *Nucl. Instrum. Methods* B **197** 185
[60] Edwards S F and Wilkinson D R 1982 The surface statistics of a granular aggregate *Proc. R. Soc.* A **381** 17
[61] Hofsäss H, Bobes O and Zhang K 2016 Argon ion beam induced surface pattern formation on Si *J. Appl. Phys.* **119** 035302